Asian Journal of Chemistry; Vol. 38, No. 7 (2026), 1805-1815
ASIAN JOURNAL OF CHEMISTRY
https://doi.org/10.14233/ajchem.2026.36058

Evaluation of Antimicrobial and Photocatalytic Degradation of Reactive Black Dye Using Fe_3O_4/rGO Nanocomposite

B.N. SURESH VARMA[1,2], P. SHYAMALA[1,*] and GANTA ANUSHA[3]

[1]Department of Chemistry, Andhra University, Visakhapatnam-530003, India
[2]Department of Chemistry, Shri Vishnu Engineering College for Women (A), Bhimavaram-534201, India
[3]Department of Engineering Physics, S.R.K.R. Engineering College, Chinaamiram, Bhimavaram-534204, India

*Corresponding author: E-mail: dr.pshyamala@andhrauniversity.edu.in

Received: 24 March 2026 *Accepted*: 30 May 2026 *Published online*: 3 July 2026 AJC-22406

The growing demand for efficient wastewater treatment technologies has intensified research into nanomaterial-based solutions capable of addressing complex environmental contaminants. In this context, the present study evaluates the performance of bare Fe_3O_4 NPs and the composite of reduced graphene oxide–iron oxide (rGO–Fe_3O_4) as advanced functional materials for wastewater purification. The desirable nanomaterials were synthesised using hydrothermal method and comprehensively characterised by X-ray diffraction analysis (XRD), scanning electron microscopy (SEM), energy dispersive X-ray spectroscopy (EDS), BET surface analyzer, X-ray photoelectron spectroscopy (XPS), Fourier transform infrared spectroscopy (FTIR) and photoluminescence spectroscopy. The average crystallite sizes of prepared Fe_3O_4 and rGO–Fe_3O_4 were determined to be 21.3 nm and 16.9 nm, respectively. This enhancement was confirmed by the superior performance of rGO–Fe_3O_4 in the degradation of reactive black (RB) dye. The optimised experiments demonstrated that 100% degradation of RB dye was attained when the process was carried out with an agitation time of 80 min, an adsorbent dose of 0.1 g, a solution pH of 12 and an initial dye concentration of 10 mg L^{-1}. Furthermore, the rGO–Fe_3O_4 nanocomposite exhibited significant antibacterial activity against *E. coli* and *S. aureus*. These findings demonstrate that rGO–Fe_3O_4 nanocomposites represent a promising multifunctional material for efficient wastewater treatment and microbial disinfection applications.

Keywords: Reduced graphene oxide, Iron oxide nanocomposites, Hydrothermal method, Reactive black dye, Antibacterial activity.

INTRODUCTION

Among carbon-based nanomaterials, graphene oxide has attracted significant interest due to its unique layered arrangement, rich oxygen-containing functional groups and remarkable surface characteristics. These properties enhance its compatibility with metal oxide nanoparticles, making it highly suitable for applications such as adsorption, sensing, catalysis and wastewater treatment [1,2]. GO based iron oxide NPs (IO NPs) particularly magnetite (Fe_3O_4) and maghemite (γ-Fe_2O_3) have attracted significant interest due to their biocompatibility, superparamagnetic, high surface activity and chemical stability [3-6]. These properties enable Fe_3O_4 and γ-Fe_2O_3 application in drug delivery, magnetic separation, environmental remediation, catalysis and imaging. However, pure IONPs tend to undergo clustering due to magnetic dipole interactions and high surface energy leading to reduced performance [7,8]. On combining IO NPs with GO develops a synergistic solution by stopping aggregation and improving electron transport, surface reactivity and chemical stability [9,10].

When iron oxide or doped iron oxides NPs like Ni, Co, Cu, Mn or Ag-doped materials when anchored onto GO sheets, the resulting hybrid nanocomposites demonstrate enhanced physico-chemical properties such as better catalytic efficiency, higher adsorption capacity, charge mobility and mechanical stability [11-13]. In this study, iron oxide nanoparticles (IO NPs) and the rGO-Fe_3O_4 nanocomposite exhibited superior photocatalytic efficiency toward the degradation of reactive black (RB) dye, along with significant antibacterial activity against *Escherichia coli* and *Staphylococcus aureus*. These findings demonstrate their dual functionality in wastewater treatment and microbial disinfection, highlighting their potential as effective nanomaterials for environmental remediation applications.

EXPERIMENTAL

Analytical reagent (AR) grade chemicals, including graphite, ferric chloride hexahydrate ($FeCl_3 \cdot 6H_2O$), sodium borohydride, sodium hydroxide, sodium nitrate, potassium permanganate, hydrogen peroxide and sulphuric acid, with purities exceeding 98%, were obtained from Bio Chem Suppliers, India. All chemicals were used as received without further purification. Deionized double-distilled water was utilized throughout the study for the preparation of solutions and experimental analyses.

Synthesis of GO: Graphene oxide (GO) was synthesised using a modified Hummers' method [14]. Initially, 3 g of graphite flakes were ultrasonicated for 30 min to increase their surface area and improve dispersion prior to the oxidation process. Subsequently, 1 g of the sonicated graphite was mixed with 0.5 g of $NaNO_3$ and dispersed in 69 mL of conc. H_2SO_4 under continuous magnetic stirring in an ice bath, maintaining the temperature below 5 ºC. After 15 min of stirring, 3 g of $KMnO_4$ was gradually added in small portions while ensuring that the reaction temperature remained below 20 ºC to avoid excessive heat generation and facilitate controlled oxidation. Upon completion of the $KMnO_4$ addition, the ice bath was removed and the reaction mixture was stirred under reflux conditions at 35 ºC for 180 min. Thereafter, 130 mL of distilled water was slowly added to the reaction mixture and stirring was continued for an additional 1 h. To stop the oxidation reaction and reduce residual permanganate ions, 10 mL of 30% H_2O_2 was added, resulting in a distinct colour change from dark brown to yellow, indicative of successful oxidation and removal of excess MnO_4^- ions. The resulting GO product was repeatedly washed with deionized water until a neutral pH was attained, thereby eliminating residual acids and inorganic impurities. Finally, the purified GO was dried in a hot-air oven at 70 ºC overnight and stored for further characterisation and subsequent composite synthesis.

Preparation of rGO-Fe_3O_4 composite: The rGO-Fe_3O_4 nanocomposite was synthesized *via* a hydrothermal method. Initially, 50 mg of the previously synthesized graphene oxide (GO) was dispersed in deionized water and ultrasonicated for 10 min to achieve uniform exfoliation and stable dispersion. Separately, equal volumes of 0.01 M $FeCl_3 \cdot 6H_2O$ and 1 M NaOH aqueous solutions were prepared and mixed. The resulting solution was then mixed with the GO suspension, followed by the addition of a small amount of $NaBH_4$ as a reducing agent. The reaction mixture was transferred into a Teflon-lined stainless-steel autoclave, sealed and maintained at 180 ºC for 8 h to facilitate the hydrothermal synthesis of rGO-Fe_3O_4 nanocomposite. After completion of the reaction, the autoclave was allowed to cool naturally to room temperature. The obtained product was collected by centrifugation and washed several times with ethanol and deionized water to remove residual impurities and unreacted precursors.

Characterisation: X-ray diffraction (XRD) patterns were recorded using a Bruker D8 Advance A25 diffractometer with Cu*K*α radiation (λ = 1.5418 Å) over the 10º-80º 2θ range to determine the crysta-lline structure. FTIR spectra was recorded to identify functional groups by using a Bruker Alpha-II ATR-FTIR spectrometer with a ZnSe beam splitter in the 4000-500 cm^{-1} region. Surface area measurements were completed *via* BET analysis using a Quantachrome NOVA Touch 4 LX instrument with nitrogen adsorption at 77 K. TEM images were captured with a Tecnai T20 (200 kV, FEI) microscope to assess particle size and morphology. To investigate elemental composition and oxidation states XPS analysis was done by using an Omicron ESCA system (Oxford, Germany). Thermal behaviour was studied using a TGA instrument (Hitachi STA 7300) from 30 ºC to 1000 ºC. Additionally, surface morphology and particle dimensions were observed through SEM using a Quanta 450 FEG FEI microscope and a Hitachi SU1510 system operated at 10-30 kV, UV-visible spectroscopy, SYSTRONICS, 200-800 nm was used for the absorption studies.

Photocatalytic degradation: The photocatalytic degradation experiments were carried out under ambient conditions using RB dye solutions adjusted to pH 4, 7 and 12. A mercury halogen lamp fitted with four 15 W bulbs was employed as the irradiation source. For each experimental run, catalyst amounts of 20, 30, 50 and 100 mg were dispersed in 100 mL of aqueous reactive black (RB) dye solution with an initial concentration of 10 mg L^{-1}. Prior to light exposure, the suspension was stirred in the absence of illumination for 30 min to attain adsorption–desorption equilibrium between the dye molecules and the catalyst surface. Upon irradiation, 3 mL samples were collected at predetermined time intervals and centrifuged at 1000 rpm to remove suspended catalyst particles. The concentration of RB dye remaining in the supernatant was quantified by recording its absorbance at 510 nm using a visible spectrophotometer.

The percentage of dye degradation was determined using eqn. 1:

$$\text{Degradation efficiency (\%)} = \frac{C^{o}_{RB} - C_{RB}}{C^{o}_{RB}} \times 100 \qquad (1)$$

where C^{o}_{RB} is the initial concentration of RB dye and C_{RB} is the concentration of RB dye at a certain irradiation time. The decrease in dye concentration with irradiation time under visible light was used to assess the photocatalytic activity of the catalyst samples.

Antimicrobial activity: The antimicrobial activity of the specimens was determined using the agar well diffusion method as described by Perez *et al.* [15]. Sterile cotton swabs were used for evenly distributing microbial inoculum across the surface of the solidified Müller-Hinton agar plates. In a sterile manner wells were punched into the agar and aliquots of the test samples (100 μg/mL, 50 μg/mL and 10 μg/mL) prepared from a 1 mg/mL stock solution, introduced into the respective wells. The inoculated agar plates containing *E. coli* and *S. aureus* were incubated at 37 ºC for 24 h under controlled conditions. Following incubation, antimicrobial activity was assessed by measuring the diameter of the clear zones of inhibition surrounding each well.

RESULTS AND DISCUSSION

X-ray diffraction (XRD) analysis: Fig. 1 displays the X-ray diffraction (XRD) patterns of Fe_3O_4, GO and the rGO-

Fe_3O_4 nanocomposite *via* hydrothermal method. The Fe_3O_4 sample shows different diffraction peaks at 2θ = 30.1º, 35.5º, 43.1º, 53.4º, 57.0º and 62.6º indexed to the (220), (311), (400), (422), (511) and (440) planes. The diffraction peaks obtained were found to be in good agreement with the characteristic cubic spinel structure of magnetite. Furthermore, the crystal plane reflections closely matched the standard values provided in JCPDS card No. 19-0629, indicating the successful formation of highly crystalline Fe_3O_4 nanoparticles [16]. This agreement confirms the successful synthesis of crystalline Fe_3O_4 nanoparticles. GO shows a broad diffraction feature centered around 10-11º, corresponding to the (001) plane which is characteristic of stacked GO layers containing oxygenated groups. The Fe_3O_4-rGO composite exhibits the characteristic of Fe_3O_4 peaks with no evident GO peak at 10-11º. The disappearance of the characteristic GO peak indicates the successful reduction of graphene oxide (GO) into reduced graphene oxide (rGO) during the hydrothermal synthesis of the composite. Furthermore, the Fe_3O_4 peaks in the composite appear with enhanced intensity, suggesting improved crystallinity and strong interaction between Fe_3O_4 nanoparticles and rGO sheets. The existence of well-defined composite pattern confirms that Fe_3O_4 nanoparticles remain structurally intact and are successfully anchored on to the rGO matrix.

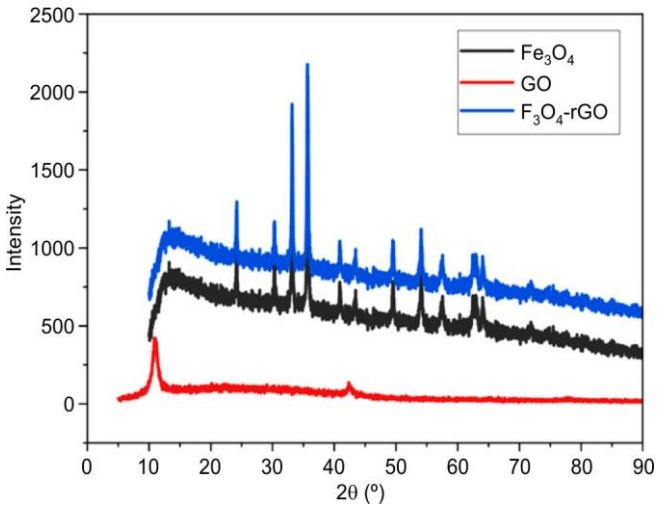

Fig. 1. XRD patterns of Fe_3O_4, GO and rGO-Fe_3O_4 nanocomposite

The average crystalline size(D) of hydrothermally prepared material was measured by Debye-Scherer formula (eqn. 2) and the average crystalline size of the Fe_3O_4 nanoparticles is obtained as 21.3 nm and the rGO-Fe_3O_4 nanocomposite is calculated and found to be 16.9 nm. No additional peaks were observed between the characteristic diffraction peaks, indicating the absence of detectable impurity phases and confirming the high purity of the synthesised material.

$$D = \frac{K\lambda}{\beta \cos\theta} \quad (2)$$

where λ denotes the wavelength of the incident X-ray radiation; K is the Scherrer constant (typically taken as 0.94); β represents the full width at half maximum (FWHM) of the diffraction peak (in radians) and θ corresponds to the Bragg diffraction angle.

FTIR analysis: Fig. 2 depicts the FTIR spectra of GO, Fe_3O_4 and Fe_3O_4/rGO nanocomposite. The FTIR spectrum of GO represents characteristic vibrational bands of oxidised graphene materials along with a broad O–H stretching band near 3400 cm^{-1} along with peaks at 1720 cm^{-1} (C=O stretching), 1620 cm^{-1} (C=C skeletal vibrations) and 1050 cm^{-1} (C–O stretching). These features confirm the existence of oxygenated functional groups and the layered structure for GO. Pure Fe_3O_4 exhibits strong absorption bands below 600 cm^{-1}, which correspond to Fe–O stretching vibrations associated with the spinel ferrite lattice. The distinct peaks around 580-590 cm^{-1} and 450 cm^{-1} indicate Fe–O bonds at tetrahedral and octahedral sites confirming the formation of magnetite. In the rGO-Fe_3O_4 composite, the intensity of GO's oxygen-related bands remarkably decreases demonstrating that GO has been partially reduced during composite formation. At the same time, the Fe–O band near 580 cm^{-1} remains prominent confirming that Fe_3O_4 nanoparticles are successfully anchored onto the rGO sheets [17]. The observed variations in band intensity indicate the successful reduction of GO to rGO, along with the formation of strong interfacial coupling between Fe_3O_4 nanoparticles and the graphene framework.

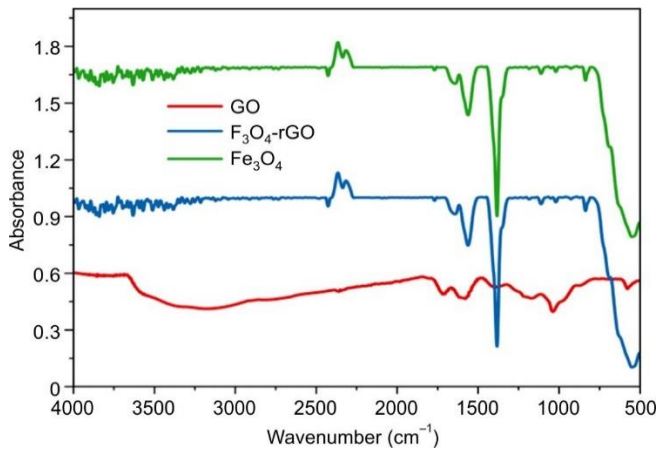

Fig. 2. FTIR patterns of Fe_3O_4, GO and rGO-Fe_3O_4 nanocomposite

Scanning electron microscopy: As shown in Fig. 3a-d, the surface morphology of the synthesized rGO-Fe_3O_4 nanocomposites was investigated using SEM analysis. The low-magnification SEM image (Fig. 3a) reveals a wrinkled sheet-like structure characteristic of rGO, decorated with Fe_3O_4 NPs, confirming the successful anchoring of Fe_3O_4 onto the rGO framework. At higher magnification (Fig. 3b), Fe_3O_4 NPs with nearly spherical to polyhedral morphologies are observed to be uniformly distributed across the graphene surface. The intermediate-magnification image (Fig. 3c) further demonstrates a dense and homogeneous coating of Fe_3O_4NPs on the rGO sheets, which effectively prevents graphene restacking while increasing the available active surface area [18]. The high-resolution SEM micrograph (Fig. 3d) shows well-defined Fe_3O_4 nanoparticles strongly anchored to the conductive rGO matrix, with particle sizes predominantly in the range of 20-50 nm and occasional larger aggregates measuring 60-80 nm. The uniform distribution of Fe_3O_4 NPs on the rGO nanosheets is expected to provide a high surface area, enhanced electrical conductivity and improved structural stability.

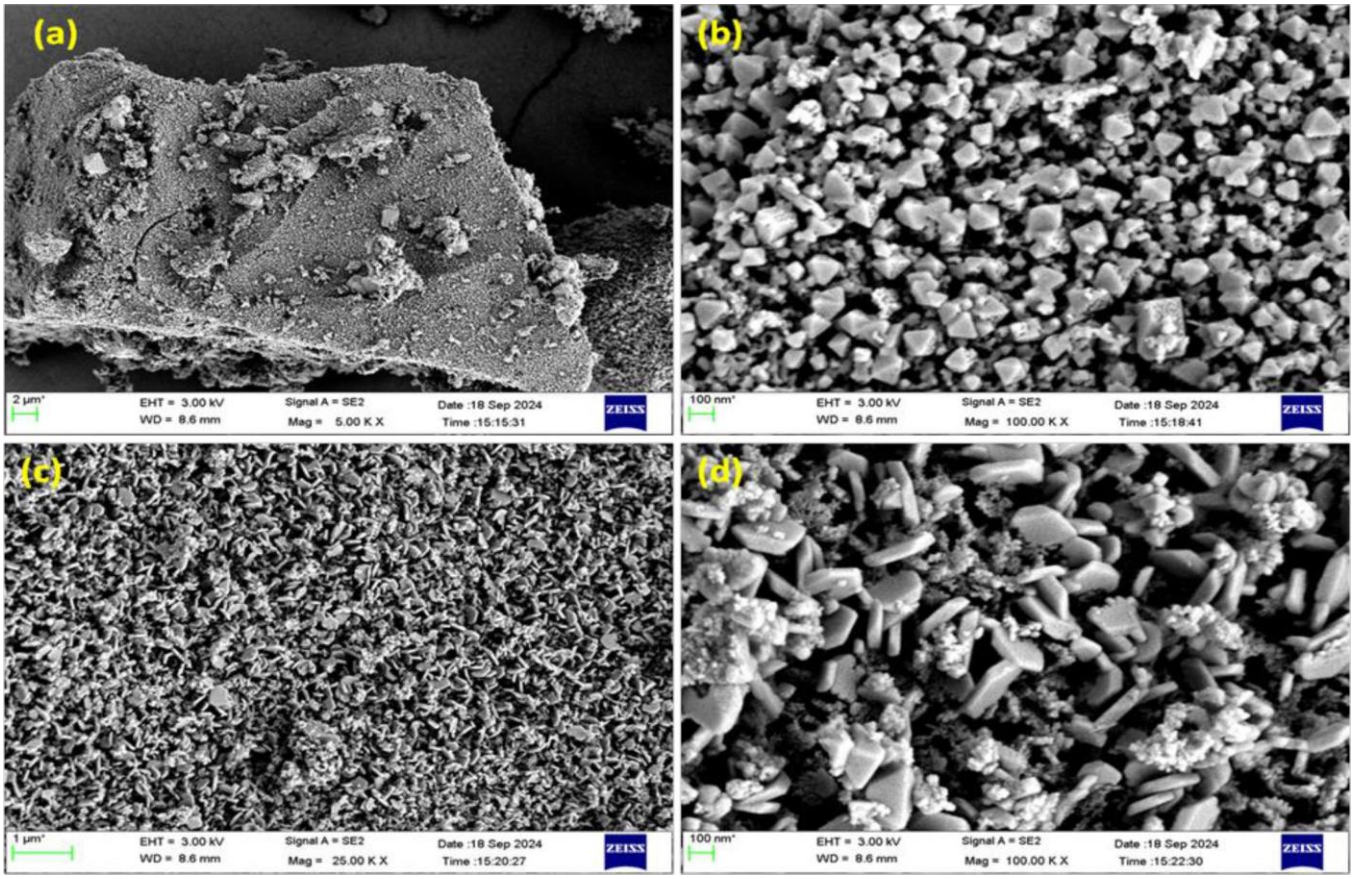

Fig. 3. SEM images of (a,b) Fe_3O_4, and (c,d) rGO-Fe_3O_4 nanocomposite

EDS analysis: Fig. 4 illustrates the EDS spectrum of the synthesized Fe_3O_4 nanoparticles. The spectrum displays prominent peaks corresponding to iron (Fe) and oxygen (O), confirming the successful formation of the iron oxide phase. Characteristic Fe peaks are observed at approximately 6.4 keV (Fe Kα) and 7.0 keV (Fe Kβ), while the O peak appears near 0.5 keV, which is typical of metal oxide materials. The absence of any additional elemental peaks indicates the high purity of the synthesized nanoparticles. Quantitative EDS analysis reveals elemental contents of approximately 72 wt.% Fe and 28 wt.% O, which are consistent with the expected composition of magnetite (Fe_3O_4) [19]. These findings confirm the successful synthesis of phase-pure Fe_3O_4 NPs and demonstrate the effectiveness of the adopted preparation method.

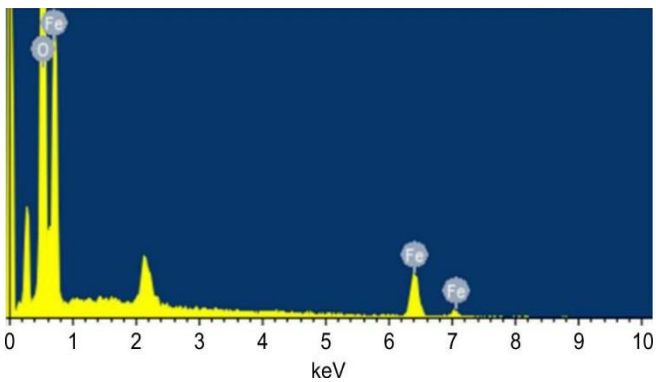

Fig. 4. EDS analysis of Fe_3O_4 nanocomposite

TEM analysis: The microstructural characteristics of the synthesized rGO-Fe_3O_4 nanocomposite were investigated using TEM analysis, and the corresponding images are shown in Fig. 5a-d. The low-magnification TEM image (Fig. 5a) reveals sheet-like rGO structures decorated with Fe_3O_4 NPs. The high-magnification image (Fig. 5b) shows that the Fe_3O_4 NPs are uniformly distributed and firmly anchored onto the wrinkled rGO sheets, with minimal particle agglomeration. The intimate interfacial contact between the Fe_3O_4 NPs and the rGO matrix suggests effective nucleation and growth of the nanoparticles on the graphene framework, which is expected to enhance structural stability and facilitate electron transport [20]. The selected area electron diffraction (SAED) pattern (Fig. 5c) exhibits a series of concentric diffraction rings indexed to the (220), (311), (400), (422), (511) and (440) crystallographic planes of cubic Fe_3O_4, confirming the polycrystalline nature and preserved crystallinity of the nanoparticles after composite formation. The particle size distribution histogram (Fig. 5d) indicates a narrow size distribution, with most Fe_3O_4 nanoparticles falling within the 18-22 nm range and an average particle size of approximately 20 nm. The nanoscale particle size, homogeneous dispersion of Fe_3O_4 NPs and strong interaction with the conductive rGO network are expected to provide a large active surface area, efficient electron transport pathways and enhanced structural stability, thereby significantly improving the electrochemical performance of the rGO-Fe_3O_4 nanocomposite.

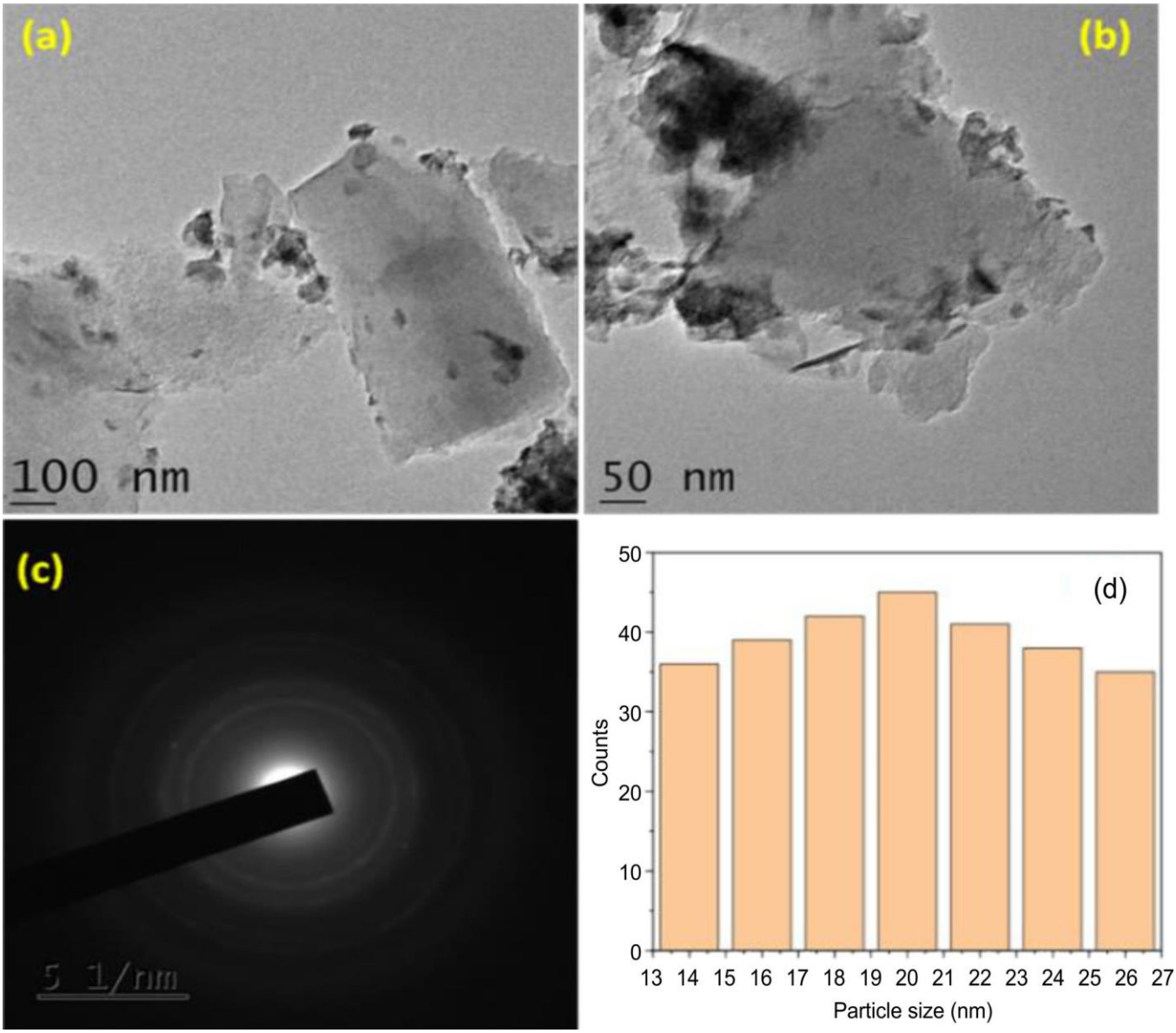

Fig. 5. (a,b) TEM images, (c) SAED patter of rGO-Fe_3O_4 nanocomposite and (d) average particle size of rGO-Fe_3O_4 nanocomposite

BET surface area and porosity analysis: The characteristics of Fe_3O_4 and rGO-Fe_3O_4 nanocomposite were quantitatively estimated using N_2 adsorption-desorption measurements at 77 K. Clear differences in the surface area and pore properties are observed between two samples highlights the influence of rGO incorporation on the structural properties (Fig. 6). For iron oxide, the BET surface area was calculated to be 17.10 $m^2\ g^{-1}$ with a monolayer adsorption capacity (V_m) of 3.93 cm^3 (STP) g^{-1}. The total pore volume determined at a relative pressure (P/P_o) of 0.99 was 0.05 $cm^3\ g^{-1}$ and the mean pore diameter was 10.75 nm indicating the leading presence of mesoporous structures with relatively larger pore sizes. The BET constant (C) value of 157.95 suggests moderate adsorbent–adsorbate interactions.

In contrast, the rGO-Fe_3O_4 nanocomposite exhibits a markable enhanced BET surface area of 125.00 $m^2\ g^{-1}$ nearly seven times higher than that of pure iron oxide [21]. The monolayer adsorption capability significantly increases to 28.66 cm^3 (STP) g^{-1} shows the availability of significant number of adsorption sites. The total pore volume also increases to 0.15 $cm^3\ g^{-1}$ while the mean pore diameter decreases to 4.76 nm indicating the formation of smaller and more uniformly distributed mesopores. The decrease in pore diameter shows the development of slit-like pores arising from the layered structure of rGO. The significant increase in the surface area and pore volume observed for the rGO-Fe_3O_4 composite can be attributed to the high intrinsic surface area of rGO, which controls nanoparticle clustering and promotes uniform dispersion of Fe_3O_4 particles [22]. The integration of rGO enhanced pore accessibility and minimised the agglomeration of Fe_3O_4 particles, resulting in improved surface area and better adsorption performance. Although the BET constant (C) value for the composite appears negative and this behaviour can be associated with surface heterogeneity and some deviations from ideal BET assumptions were observed in graphene-based materials.

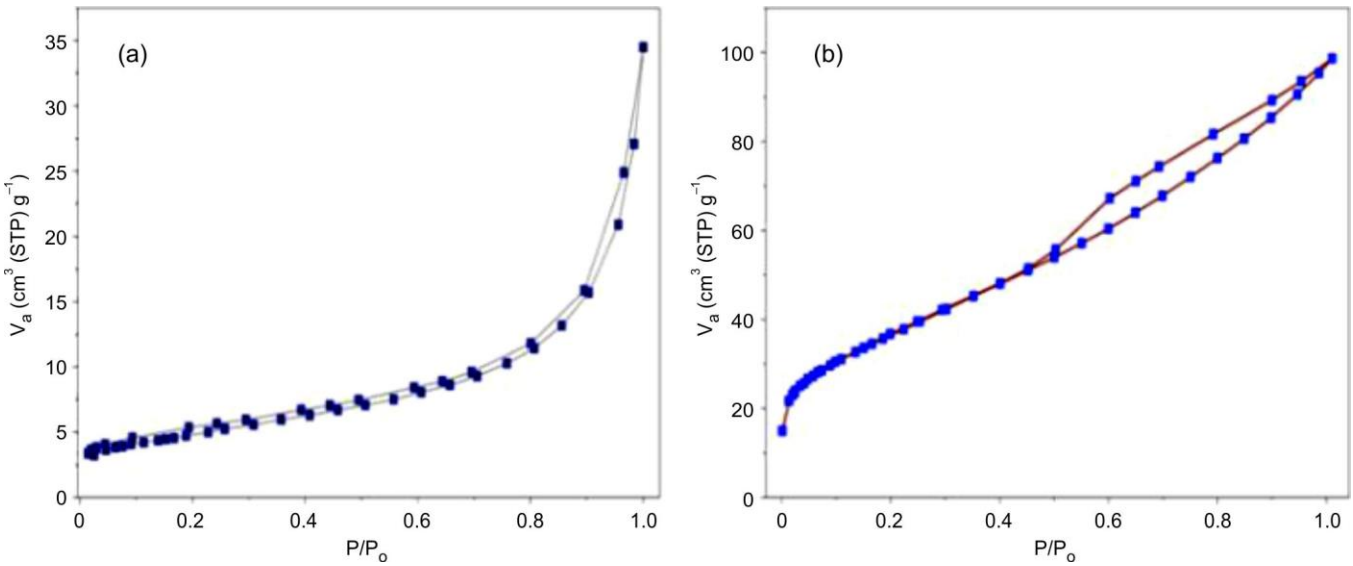

Fig. 6. The adsorption/desorption plots of Fe_3O_4 and rGO-Fe_3O_4 nanocomposite

XPS analysis: XPS technique was employed to examine the elemental composition and chemical states of the rGO-Fe_3O_4 nanocomposite (Fig. 7). The survey spectrum confirms the presence of Fe, O and C elements without any detectable impurity signals, indicating the successful synthesis of a high purity nanocomposite [23]. The high-resolution Fe 2p spectrum exhibits characteristic peaks at 710.8 eV (Fe $2p_{3/2}$) and 724.5 eV (Fe $2p_{1/2}$), confirming the coexistence of Fe^{2+} and Fe^{3+} species typical of the Fe_3O_4 phase. In the O 1s spectrum, the peak at 529.9 eV is attributed to lattice oxygen in Fe–O bonds, while the shoulder at 531.5 eV corresponds to oxygen-containing functional groups (C–O and C=O) on the rGO surface.

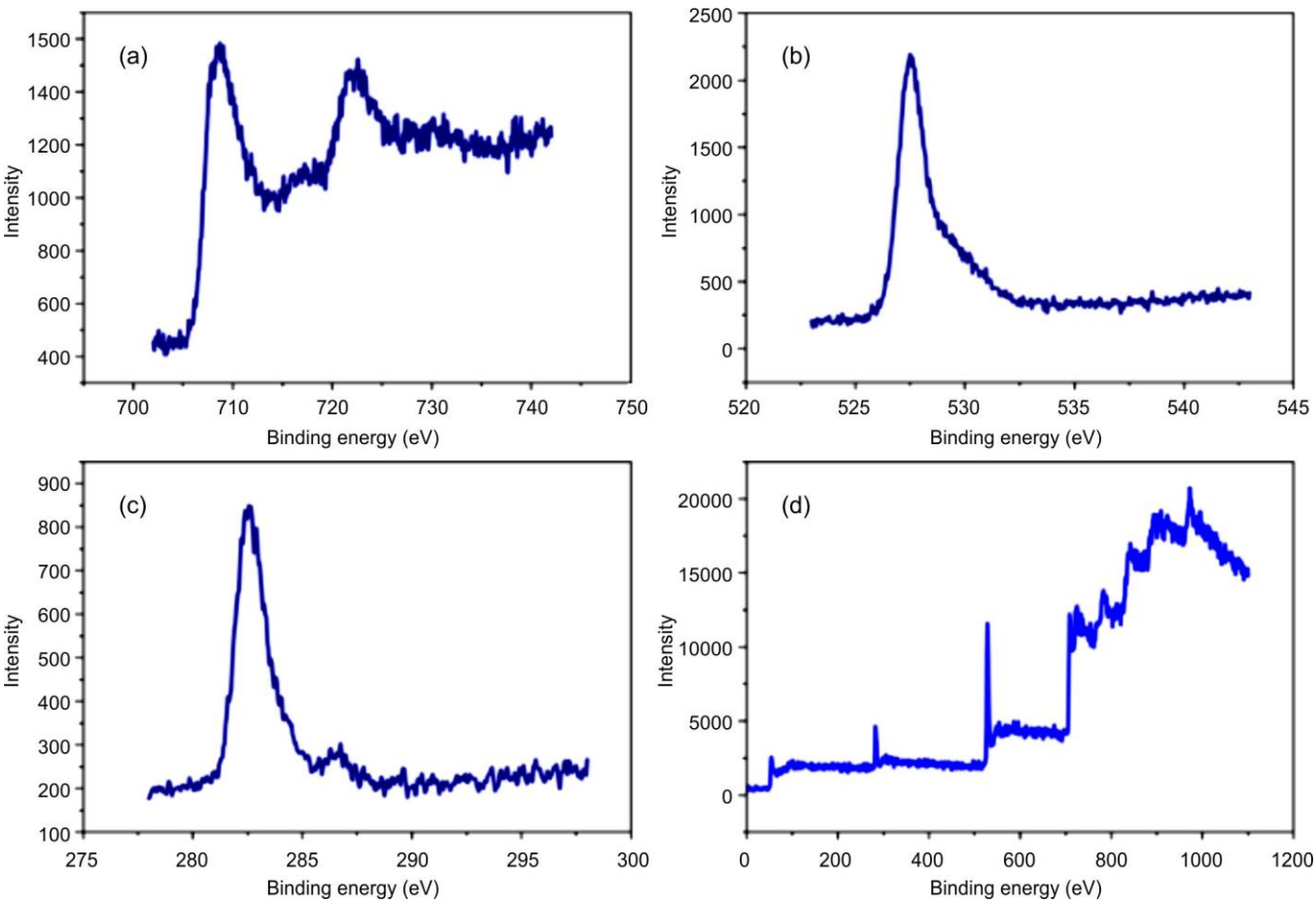

Fig. 7. XPS data (a) Fe $2p_{3/2}$, (b) O 1s, (c) C 1s and (d) survey Fe_3O_4 nanocomposite

The C 1s spectrum shows a dominant peak at 284.6 eV associated with sp^2-hybridized graphitic carbon (C=C/C–C). Additional weak peaks at 286.2 eV and 288.4 eV are assigned to C–O and O–C=O groups, respectively, indicating partial reduction of graphene oxide [23]. These findings confirm the successful formation of the rGO-Fe_3O_4 nanocomposite with preserved graphitic structure and Fe_3O_4 functionality

Thermal analysis: The TGA-DTA profile of the rGO-Fe_3O_4 nanocomposite is consistent with the thermal behaviour of graphene-based metal oxide composites. An initial weight loss of 1.3% below 120 ºC is attributed to the removal of physically adsorbed moisture, reflecting the high surface area and hydrophilic nature of the material. A gradual mass loss of 3.8% up to 300 ºC corresponds to the decomposition of residual oxygen-containing functional groups, such as hydroxyl, epoxy and carboxyl groups, present on the rGO surface. The broad DTA peak centered around 320 ºC is associated with the thermal reduction and structural rearrangement of graphene based components, indicating controlled thermal transformation rather than abrupt degradation [24,25]. A further weight loss of 7.8% between 300 ºC and 456 ºC is attributed to the decomposition of the carbonaceous framework of rGO, representing the primary degradation stage of the composite. Beyond 500 ºC, only minor mass loss is observed, demonstrating the excellent thermal stability of the Fe_3O_4 matrix. The negligible weight changes above 700 ºC and absence of significant DTA signals indicate the lack of further phase transitions or decomposition reactions. The total weight loss of approximately 18-19% confirms the expected rGO content, while the high residual mass highlights the thermal robustness of the iron oxide framework (Fig. 8).

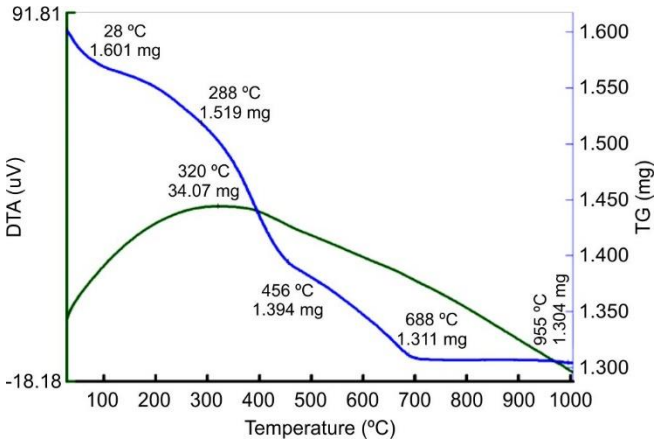

Fig. 8. Thermograms of rGO-Fe_3O_4 nanocomposite

Photoluminescence analysis: The photoluminescence (PL) spectra obtained during the degradation of reactive black dye in the presence of the rGO–Fe_3O_4 composite reveal a progressive increase in emission intensity with prolonged irradiation time over an 80 min duration, as shown in Fig. 9. At the beginning of the reaction (0 min), the spectrum displays minimal emission intensity with no distinct peak, which can be associated with the strong fluorescence quenching effect of the intact reactive black dye molecules. As the photocatalytic process advances, a weak emission band gradually emerges around 420 nm after 50 min, suggesting the formation of

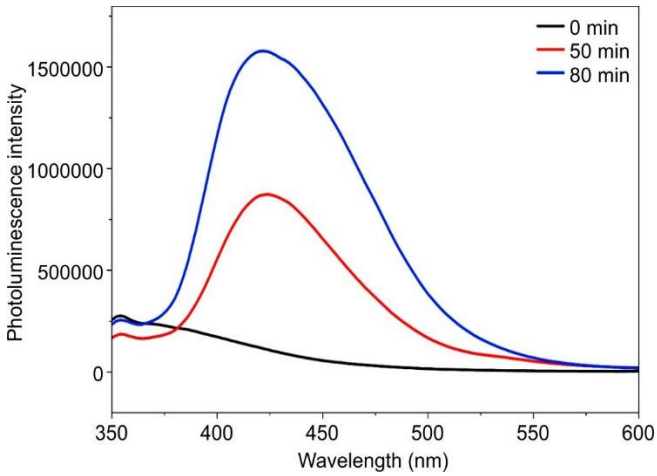

Fig. 9. PL emission spectra of the rGO-Fe_3O_4 nanocomposite photocatalyst and its interaction with RB dye at different periods

fluorescent degradation products. A significant rise in PL intensity is observed at 80 min, indicating extensive dye decomposition. The continuous enhancement in photoluminescence intensity confirms the effective photocatalytic performance of the rGO–Fe_3O_4 composite, which may be attributed to dye breakdown, diminished quenching effects and the formation of fluorescent aromatic intermediates emitting within the violet–blue region of the spectrum [26].

Degradation of RB dye: The photocatalytic activity of the synthesised Fe_3O_4 and rGO-Fe_3O_4 nanocomposite was analysed under visible-light irradiation using RB dye as the target pollutant at neutral pH. When the experiment was first conducted with only Fe_3O_4 nanoparticles, the degradation efficiency of 39.6% was attained after 80 min of irradiation. As expected, the combination of rGO significantly improved the catalytic efficiency. Under same operating conditions 50 mg catalyst dosage and 10 ppm initial dye concentration the rGO-Fe_3O_4 nanocomposite exhibited higher degradation efficiency compared to Fe_3O_4 alone. To achieve complete degradation of RB dye using the catalyst rGO-Fe_3O_4 optimisation of the reaction parameters was important. Variables such as solution pH, photocatalyst dosage and initial dye concentration were systematically adjusted to determine the most effective operational conditions for maximum photocatalytic efficiency.

The degradation of RB dye in the presence of Fe_3O_4 NPs over different time intervals at pH-7 is illustrated by the visible absorption spectra as shown in Fig. 10b. The initial absorption peak observed at 611 nm corresponds to the band of the dye. As the reaction time runs from 0 to 80 min gradual decrease in the absorption intensity is clearly observed indicating the decomposition of the dye molecules. The continuous decline in absorbance describes the catalytic activity of Fe_3O_4 which effectively facilitates the degradation process. This time dependent decline confirms that Fe_3O_4 NPs play a vital role as an efficient catalyst in promoting dye removal and highlighting their potential application in wastewater treatment.

Effect of pH: The degradation efficiency of RB dye increases with pH showing 39% degradation at pH-4, 45.17% at pH-7 and 72.87% at pH-12 as shown in the Fig. 10a-c. This pattern indicates that alkaline factors are more favourable for dye degradation. The improved performance is due to the

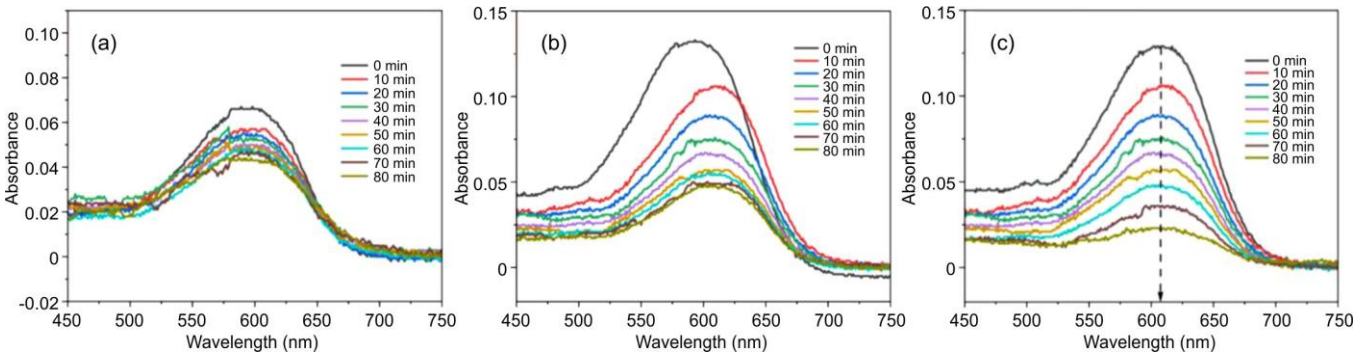

Fig. 10. Photocatalytic degradation efficiency of RB dye under different pH conditions

hydroxyl radical (•OH) formation is increased and oxidation potential. In contrast, under the acidic conditions smaller numbers of hydroxyl radicals are available leading to minimal degradation efficiency. To further optimizing the process, increasing the pH value beyond 9 could enhance degradation although excessively high pH levels (>11) might stabilize the dye or interfere with catalyst activity.

Effect of initial dye concentration: The effect of the initial dye concentration on the photocatalytic performance of the rGO–Fe_3O_4 nanocomposite was systematically investigated under optimised pH conditions, while maintaining a constant irradiation time of 80 min. By using RB dye solutions with initial concentrations of 5, 10, 20 and 30 ppm experiments were conducted. Before irradiation, the dye catalyst suspensions were kept in dark for 30 min to establish the adsorption–desorption equilibrium. Almost 25% removal of the dye was observed during this dark adsorption stage for all concentrations chosen.

Following equilibrium, the visible-light irradiation was applied and the degradation process was observed with irradiation time considered as t = 0. The complete degradation was completed within 90 min for 5 ppm solution, whereas 30 ppm sample required approximately 80 min to achieve complete degradation. As shown in Fig. 11, the photocatalytic efficiency of the rGO-Fe_3O_4 catalyst was decreased as the initial dye concentration increased. Higher concentrations of RB dye results in a larger number of dye molecules occupying the catalyst surface, which limits the light penetration and restricts the generation of reactive species like hydroxyl radicals. Therefore, the minimal availability of the hydroxyl radicals leads to lowers the photocatalytic degradation efficiency at increased dye concentrations.

Effect of catalyst dose: The influence of catalyst loading on RB dye degradation was examined while maintaining all other experimental parameters constant. The photocatalytic experiments were conducted using varying amounts of rGO-Fe_3O_4 catalyst 20, 30, 50 and 100 mg at a fixed dye concentration of 10 mg L^{-1}. Complete degradation was achieved within 150, 120, 100 and 70 min, respectively as shown in Fig. 12. An increase in the catalyst dosage enhanced the photocatalytic performance, primarily due to greater photon absorption and a higher number of reactive sites available for dye molecule interaction.

Mechanistic studies: The contribution of different reactive oxygen species (ROS) to the photocatalytic degradation of

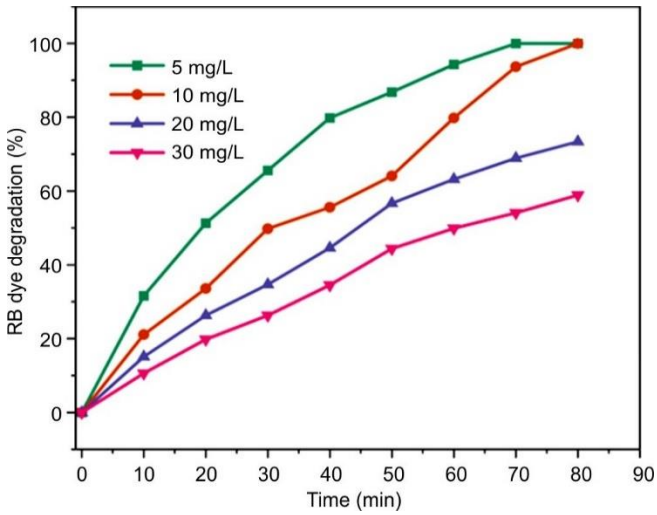

Fig. 11. Photocatalytic degradation of RB dye under different initial dye concentrations

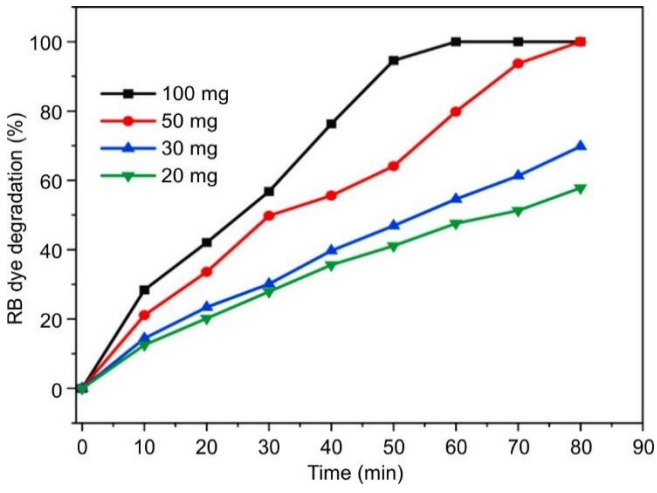

Fig. 12. Photocatalytic degradation performance of RB dye using different catalyst dosages

reactive black (RB) dye was investigated through trapping experiments using selective scavenging agents, as shown in Fig. 13. In the absence of any quenchers, complete degradation (100%) of the dye was achieved, demonstrating the excellent photocatalytic efficiency of the rGO-Fe_3O_4 nanocomposite under visible light irradiation. When different scavengers were allowed into the reaction system a consider-

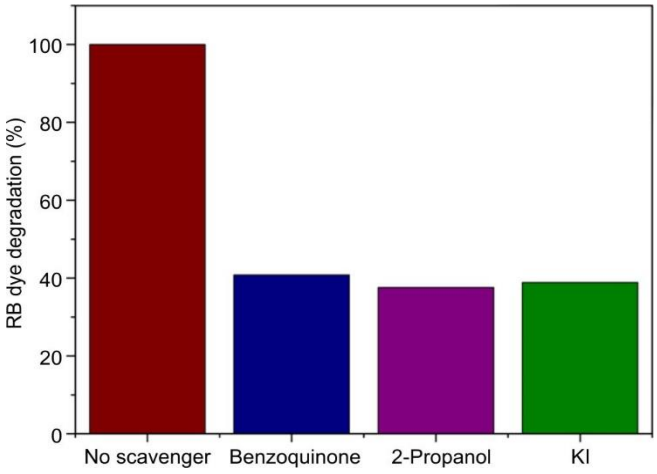

Fig. 13. Effect of different radical scavengers on the photocatalytic degradation of RB dye

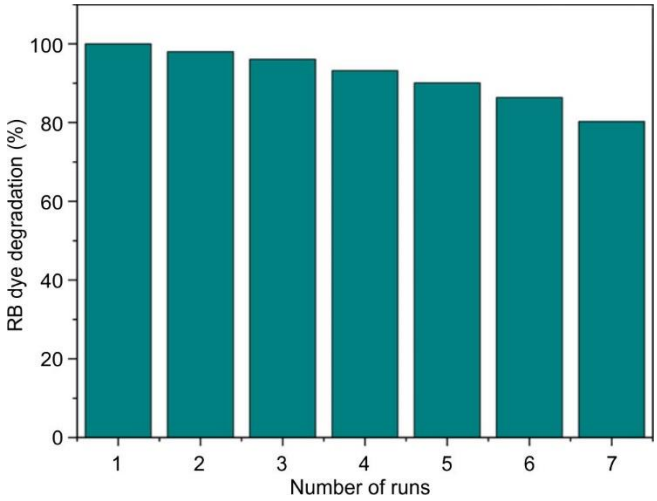

Fig. 14. Reusability data of rGO-Fe_3O_4 photocatalyst after number of runs

able reduction in photocatalytic efficiency was observed. The addition of benzoquinone decreased the degradation efficiency to 40.8%, whereas 2-propanol, which quenches hydroxyl radicals ($^{\bullet}OH$), reduced the degradation to 37.6%. Similarly, the presence of KI, a hole (h^+) scavenger, resulted in a degradation efficiency of 38.9%. The significant suppression in photocatalytic activity in all scavenger-assisted experiments clearly indicates that superoxide radicals, hydroxyl radicals and photogenerated holes play important roles in the degradation mechanism. Among the scavengers tested, KI and 2-propanol caused slightly greater inhibition than benzoquinone, suggesting that $^{\bullet}OH$ radicals and h^+ contribute more prominently to the degradation pathway, although the presence of $^{\bullet}O_2^-$ radicals is also essential.

Reusability and stability: As shown in Fig. 14, the long-term reusability and stability of the rGO-Fe_3O_4 catalyst were studied through repeated RB dye degradation cycles under optimised conditions. The catalyst maintained high photocatalytic efficiency over multiple successive cycles, demonstrating good stability and reusability. These results highlight its suitability for practical applications in wastewater treatment. In the first cycle, the complete degradation (100%) of RB dye was attained. Slight decrease in efficiency was observed in several cycles with degradation efficiencies of 98%, 96.1%, 93.2% and 90.1% recorded from second to fifth cycles. Further cycles showed moderate decrease with efficiencies of 86.4% in the sixth run and 80.3% in the seventh run. A gradual decline in performance occurred with repeated use the catalyst retained more than 80% of its initial activity even after seven cycles. The slight decline in degra dation efficiency can be ascribed to possible surface fouling, partial deactivation or blockage of active sites and minor loss of catalyst mass during the separation and recovery steps.

Mechanism of degradation of RB dye: The pH of the reaction medium is a key factor in photocatalytic processes occurring on solid catalyst surfaces, as it directly affects the surface charge of the photocatalyst and the extent of particle aggregation in solution. Changes in pH also modify the chemical form and stability of dye molecules, thereby influencing the dominant degradation pathways. These pathways may include oxidative attack by hydroxyl radicals, direct oxidation by photogenerated holes and reduction reactions mediated by conduction band electrons. When irradiated with visible light, the photocatalyst becomes photoactivated and generates electron-hole pairs across its surface. The positively charged holes (h^+), exhibiting strong oxidizing properties, participate in the direct oxidation of dye molecules or promote the formation of hydroxyl radicals ($^{\bullet}OH$) through interactions with OH^- ions and water molecules. Meanwhile, conduction band electrons (e^-) can react with dissolved oxygen to form superoxide radical species ($O_2^{\bullet-}$). These reactive oxygen species subsequently contribute to the degradation of dye molecules, leading to their conversion into simpler and environmentally harmless end products such as CO_2 and H_2O. This degradation efficiency was further supported by the COD analysis, which yielded a value of 87 mg/L. These reactive oxygen species subsequently participate in the degradation of dye molecules, ultimately breaking them down into simpler, environmentally benign products such as CO_2 and H_2O, which were confirmed by COD result obtained with 87 mg/L.

$$\text{Semiconductor} + h\nu \rightarrow (\text{Semiconductor})\, e^-_{CB} + h^+_{VB} \quad (3)$$

$$h^+_{VB} + \text{Dye} \rightarrow \text{Dye}^{\bullet+} (\text{oxidation of the dye}) \quad (4)$$

$$h^+_{RB} + OH^- \rightarrow OH^{\bullet}$$

$$OH^{\bullet} + \text{Dye} \rightarrow \text{Degradation of the dye} \rightarrow CO_2 + H_2O \quad (5)$$

Table-1 compares the photocatalytic degradation performance of RB dye using various graphene- and carbon-based nanocomposites synthesized through different methods. Among the reported materials, the hydrothermally synthesized rGO-Fe_3O_4 nanocomposite achieved complete dye degradation (100%) within 80 min under visible-light irradiation, outperforming previously reported catalysts. This enhanced performance can be attributed to the synergistic interaction between rGO and Fe_3O_4, which promotes efficient charge separation and improves photocatalytic activity.

Antibacterial activity: The antibacterial activity of the rGO-Fe_3O_4 nanocomposite and Fe_3O_4 nanoparticles was evaluated against Gram-positive *S. aureus* and Gram-negative *E. coli* using the zone of inhibition assay at different concentrations. Against *S. aureus*, the control exhibited an inhibition

TABLE-1
COMPARATIVE ANALYSIS OF METAL OXIDE NANOCOMPOSITE FORMATION METHODS AND THEIR DYE DEGRADATION EFFICIENCIES

Nanocomposite catalyst	Synthesis method	Light source	Reaction time (min)	Degradation (%)	Ref.
TiO_2/graphene oxide	Sol gel	UV	90	83	[27]
ZnO/rGO	Hydrothermal	Visible	80	91	[28]
Fe_3O_4/graphene	Co-precipitation (deposition–precipitation)	Visible	80	88	[29]
NiO–carbon composite	Hydrothermal	Visible	70	92	[30]
rGO-Fe_3O_4	Hydrothermal	Visible	80	100	Present study

zone of 30 mm. The rGO-Fe_3O_4 nanocomposite exhibited superior antibacterial activity against the Gram-positive *S. aureus*, achieving a maximum inhibition zone of 28 mm at 100 µg/mL, whereas Fe_3O_4 nanoparticles produced a smaller inhibition zone of 22 mm under the same conditions. In contrast, Fe_3O_4 nanoparticles showed greater effectiveness against the Gram-negative *E. coli*, with inhibition zones ranging from 18-25 mm, while the rGo-Fe_3O_4 nanocomposite displayed limited activity (Table-2). These differences are likely associated with variations in bacterial cell wall structure and the distinct interactions of the nanomaterials with microbial membranes.

TABLE-2
ANTIBACTERIAL ACTIVITY DATA OF Fe_3O_4 AND rGO-Fe_3O_4 SAMPLES

Test micro-organism	rGO-Fe_3O_4		Fe_3O_4	
	Conc. (µg/mL)	ZOI (mm)	Conc. (µg/mL)	ZOI (mm)
S. aureus	Control	30	Control	30
	100	28	100	22
	50	22	50	20
	10	15	10	15
E. coli	Control	15	Control	26
	100	15	100	25
	50	13	50	22
	10	0	10	18

Conclusion

The successful incorporation of rGO for the formation of rGO-Fe_3O_4 NPs was achieved through hydrothermal method approach. The photocatalytic degradation of RB dye in the visible light irradiation using Fe_3O_4 and rGO-Fe_3O_4 composite were examined and these results shown that the synthesised rGO-Fe_3O_4 were more effective for RB dye degradation. The degradation studies were observed at pH- 4, 7 and 12. At pH-12 the photocatalytic dye degradation is found to be 100% within a span of 80 min. The obtained results show that rGO-Fe_3O_4 are suitable in degradation of RB dye for wastewater treatment in large scale. The antibacterial study revealed that rGO-Fe_3O_4 exhibited better activity against *S. aureus*, showing inhibition zones of 28, 22 and 15 mm at 100, 50 and 10 µg/mL, respectively, compared to Fe_3O_4 (22, 20 and 15 mm). In contrast, Fe_3O_4 demonstrated stronger antibacterial performance against *E. coli*, with inhibition zones of 25, 22 and 18 mm at 100, 50 and 10 µg/mL, respectively, whereas rGO-Fe_3O_4 showed lower activity (15, 13 and 0 mm).

ACKNOWLEDGEMENTS

The authors gratefully acknowledge Department of Chemistry, Andhra University, Shri Vishnu Engineering College for Women, Bhimavaram and Bio Enviro Chemical Solutions, Visakhapatnam, India for providing the research facilities and instrumentation assistance.

CONFLICT OF INTEREST

The authors declare that there is no conflict of interests regarding the publication of this article.

DECLARATION OF AI-ASSISTED TECHNOLOGIES

During the preparation of this manuscript, the authors used an AI-assisted tool(s) to improve the language. The authors reviewed and edited the content and take full responsibility for the published work.

REFERENCES

1. Y. Zhu, S. Murali, W. Cai, X. Li, J.W. Suk, J.R. Potts and R.S. Ruoff, *Adv. Mater.*, **22**, 3906 (2010); https://doi.org/10.1002/adma.201001068.
2. A.K. Gupta and M. Gupta, *Biomaterials*, **26**, 3995 (2005); https://doi.org/10.1016/j.biomaterials.2004.10.012
3. S. Laurent, D. Forge, M. Port, A. Roch, C. Robic, L. Vander Elst and R.N. Muller, *Chem. Rev.*, **108**, 2064 (2008); https://doi.org/10.1021/cr068445e
4. Q. Liu, J. Chen, T. Mei, X. He, W. Zhong, K. Liu, D. Wang, Y. Wang, M. Li and D. Wang, *J. Mater. Chem. A Mater. Energy Sustain.*, **6**, 3692 (2018); https://doi.org/10.1039/C7TA10107D
5. H. Sun, Z. Xu and C. Gao, *Adv. Mater.*, **25**, 2554 (2013); https://doi.org/10.1002/adma.201204576
6. J. Zhu, M. Chen, H. Qu, H. Wei, J. Guo, Z. Luo, N. Haldolaarachchige, D.P. Young, S. Wei and Z. Guo, *J. Mater. Chem. C Mater. Opt. Electron. Devices*, **2**, 715 (2014); https://doi.org/10.1039/C3TC32007C
7. X. Zhang, S. Wang, C. Zhu, M. Liu, Y. Ji, L. Feng, L. Tao and Y. Wei, *J. Colloid Interface Sci.*, **397**, 39 (2013); https://doi.org/10.1016/j.jcis.2013.01.063
8. C.L. Hsueh, C.Y. Chen, J.R. Ku, S.F. Tsai, Y.Y. Hsu, F. Tsau and M.S. Jeng, *J. Power Sources*, **177**, 485 (2008); https://doi.org/10.1016/j.jpowsour.2007.11.096
9. D. Li and R.B. Kaner, *Science*, **320**, 1170 (2008); https://doi.org/10.1126/science.1158180
10. H. Qiao, Z. Lin, X. Sun, W. Li, Y. Zhao and C. Guo, *Sensors*, **23**, 7810 (2023); https://doi.org/10.3390/s23187810
11. X. Li, J. Zhu and H. Li, *Appl. Catal. B*, **123–124**, 174 (2012); https://doi.org/10.1016/j.apcatb.2012.04.009

12. E.A. Namikuchi, R.D.L. Gaspar, D.S. da Silva, I.M. Raimundo Jr. and I.O. Mazali, *Nano Express*, **2**, 020022 (2021); https://doi.org/10.1088/2632-959X/ac0596
13. H. Wang, J.T. Robinson, X. Li and H. Dai, *J. Am. Chem. Soc.*, **131**, 9910 (2009); https://doi.org/10.1021/ja904187v
14. A.A. Melegy, Y.K. Abdel-Monem, F.A. Ali, N.E. Maysour and A.M. Atta, *Sci. Rep.*, **15**, 40393 (2025); https://doi.org/10.1038/s41598-025-24533-3
15. C. Perez, M. Pauli and P. Bazerque, *Acta Biol. Med. Exp.*, **15**, 113 (1990).
16. M.C. Biesinger, *Appl. Surf. Sci.*, **597**, 153681 (2022); https://doi.org/10.1016/j.apsusc.2022.153681
17. Y. Zhang, W. Yang, S. Li and L. Bian, *Spectrochim. Acta A Mol. Biomol. Spectrosc.*, **249**, 119116 (2021); https://doi.org/10.1016/j.saa.2020.119116
18. W. Zhou, R. Apkarian and Z.L. Wang, in eds.: W. Zhou and Z.L. Wang, Fundamentals of Scanning Electron Microscopy (SEM), In: Scanning Microscopy for Nanotechnology, Springer, pp. 1-40 (2006).
19. D. Yoon, J. Hwang, W. Chang and J. Kim, *Chem. Eng. J.*, **317**, 890 (2017); https://doi.org/10.1016/j.cej.2017.02.108
20. I. Chowdhury, M.C. Duch, N.D. Mansukhani, M.C. Hersam and D. Bouchard, *Environ. Sci. Technol.*, **48**, 9382 (2014); https://doi.org/10.1021/es5020828
21. M. Cao, L. Zhao, D. Xu, D. Parsley, R. Ciora, P.K.T. Liu, V.I. Manousiouthakis and T.T. Tsotsis, *Chem. Eng. J.*, **420**, 127694 (2021); https://doi.org/10.1016/j.cej.2020.127694
22. M. Thommes, K. Kaneko, A.V. Neimark, J.P. Olivier, F. Rodriguez-Reinoso, J. Rouquerol and K.S.W. Sing, *Pure Appl. Chem.*, **87**, 1051 (2015); https://doi.org/10.1515/pac-2014-1117
23. D.N.G. Krishna and J. Philip, *Appl. Surf. Sci. Adv.*, **12**, 100332 (2022); https://doi.org/10.1016/j.apsadv.2022.100332
24. S.A. Khan, Z. Arshad, S. Shahid, I. Arshad, K. Rizwan, M. Sher and U. Fatima, *Compos., Part B Eng.*, **175**, 107120 (2019); https://doi.org/10.1016/j.compositesb.2019.107120
25. S.K. Mandal, K. Dutta, S. Pal, S. Mandal, A. Naskar, P.K. Pal, T.S. Bhattacharya, A. Singha, R. Saikh, S. De and D. Jana, *Mater. Chem. Phys.*, **223**, 456 (2019); https://doi.org/10.1016/j.matchemphys.2018.11.002
26. R. Saraf, C. Shivakumara, H. Nagabhushana and N. Dhananjaya and S. Behera, *Spectrochim. Acta A Mol. Biomol. Spectrosc.*, **136**, 348 (2015); https://doi.org/10.1016/j.saa.2014.09.038
27. N. Beigi, H. Shayesteh, S. Javanshir and M. Hosseinzadeh, *Environ. Res.*, **231**, 116146 (2023); https://doi.org/10.1016/j.envres.2023.116146
28. B. Tao, Z. Qian, F. Miao and P. Zhang, *Mikrochim. Acta*, **192**, 555 (2025); https://doi.org/10.1007/s00604-025-07355-y
29. N.I. Zaaba, K.L. Foo, U. Hashim, S.J. Tan, W.W. Liu and C.H. Voon, *Procedia Eng.*, **184**, 469 (2017); https://doi.org/10.1016/j.proeng.2017.04.118
30. G.M. Al-Senani, F.F. Al-Fawzan, M. Alshabanat, O.H. Abd-Elkader, M. Nasrallah and M. Nasrallah, *Crystals*, **13**, 1497 (2023); https://doi.org/10.3390/cryst13101497